Surface chemistry and buried interfaces in all-inorganic nanocrystalline solids

Emilio Scalise,[1] Vishwas Srivastava,[2] Eric M. Janke,[2] Dmitri Talapin,[2,3] Giulia Galli,[2,3,4] and Stefan Wippermann[1,*]

[1] *Max-Planck-Institut für Eisenforschung GmbH, Max-Planck-Straße 1, 40237 Düsseldorf, Germany*
[2] *Department of Chemistry and James Franck Institute, University of Chicago, Chicago, Illinois 60637, United States*
[3] *Argonne National Laboratory, Lemont, Illinois 60439, United States*
[4] *Institute for Molecular Engineering, University of Chicago, Chicago, Illinois 60637, United States*

(Dated: November 25, 2020)

Semiconducting nanomaterials synthesized using wet chemical techniques play an important role in emerging optoelectronic and photonic technologies. One of the outstanding challenges for the rational design of these systems is the control of the surface chemistry of nano-building blocks and of the buried interfaces between nanoparticles and ligands. Here we present an integrated theoretical and experimental approach to characterize, at the atomistic level, buried interfaces in solids of InAs nanoparticles capped with $Sn_2S_6^{4-}$ ligands. These prototypical, all inorganic nano-composites are known for their promising transport properties and unusual negative photoconductivity. We found that contrary to assumptions based on common knowledge of organic cappings, inorganic ligands dissociate on InAs, forming a surface passivation layer and a matrix embedding the nanocrystal. A nanocomposite with unique electronic and transport properties is then formed, exhibiting type-II heterojunctions favorable for exciton dissociation and charge separation. By means of first principles calculations, validated by experiments, we identified how the matrix density, sulfur content and specific defects may be designed to attain desirable electronic and transport properties, e. g., by creating a sulfur chain network connecting the nanoparticles. In addition we could explain the origin of the measured negative photoconductivity of the nanocrystalline-solids.

Semiconductors created by using colloidal nanocrystals (NCs) as "artificial atoms" are emerging as tunable, earth-abundant and potentially non-toxic materials for solar energy conversion, light emission and electronic applications. Recent advances in wet chemical techniques [1–3] enabled the synthesis of NCs with controlled shape [4] and composition [5]. Colloidal techniques also permitted to assemble NCs into superlattices, thus leading to scalable solution-based approaches for designing solids with tailored properties [6–11]. The electronic and transport properties of nanocrystal-based solids depend on many factors, encompassing the intrinsic characteristics of the individual NCs, e. g. their shape, size, composition, as well as their surface chemistry and mutual interactions.

Organic ligands traditionally used in NC synthesis [12], play a central role in controlling shape and size, as well as in driving self-assembly into superlattices [3, 13]. However, these ligands are often composed of long hydrocarbon chains, which create an insulating barrier leading to low charge carrier mobilities [14]. Significantly higher mobilities could be achieved by using inorganic ligands. For example molecular metal chalcogenide complexes (MCCs), including $Sn_2S_6^{4-}$, $In_2Se_4^{2-}$, AsS_3^{3-} or $Cu_7S_4^{1-}$ [6, 15, 16] were used to cap CdSe, CdTe, PbS, InAs or InP NCs, forming stable solutions in polar solvents and leading to the formation of semiconducting media surrounding the NCs [15–18]. The introduction of inorganic ligands enabled significant performance improvements of NC-based solar cells [19], transistors [20], and lasers [21]. In particular MCC-capped InAs and CdSe NCs were shown to exhibit high electron mobilities [16, 22–25], with III-V based nanomaterials preferable for commercial applications, due to lower toxicity. However the atomistic structure of these materials remains poorly understood, in particular that of the NC surfaces and interfaces, whose control is required to engineer systems with desired properties. Our work provides a strategy for modeling a broad class of nanocrystal-in-glass systems [26–28], extending significantly beyond semiconductor quantum dots and MCC ligands.

At present, probing buried nano-interfaces is extremely challenging. Most experiments rely on nuclear magnetic resonance (NMR) or infrared spectroscopy. While these techniques provide essential information on the composition of the medium surrounding the NCs, they are ineffective to probe nanointerfaces at the atomistic level. On the theoretical side, models used in the literature have so far considered highly idealized NCs, where the surface atoms are located close to their bulk equilibrium positions and the ligands are adsorbed as intact structural units. Such models are unable to capture the full structural complexity of nanomaterials.

Here we focused on InAs NCs capped with $Sn_2S_6^{4-}$ ligands as prototypical nanocomposites exhibiting promising transport properties, e.g. high mobilities measured by field-effect (FET) transconductance, in addition to an unexplained switching between positive and negative photoconductivity [16] (Fig. 1). By combining electronic structure calculations and first principles molecular dynamics (MD) simulations with experiments, we show that the ligands are not absorbed as intact units but rather they decompose upon contact with the NC surface, form-

* wippermann@mpie.de

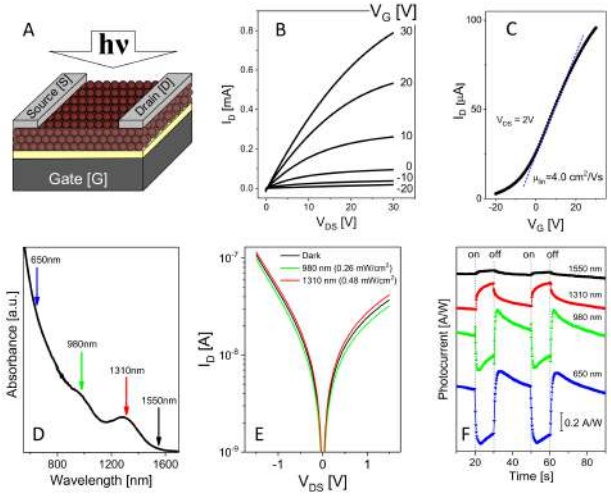

Figure 1. Measured electronic and optical properties of layers of 4.5nm InAs NCs capped with $Sn_2S_6^{4-}$ ligands. **a)** Experimental setup for the field-effect mobility and photoconductivity measurements. Heavily-doped Si wafers were used as substrates and gate terminals, 100 nm thick thermally grown SiO_2 layers (yellow) served as gate dielectrics. Aluminum source and drain electrodes were evaporated on top of the NC film. **b,c)** The output b) and transfer c) characteristics of a field-effect transistor assembled from InAs NCs capped with $Sn_2S_6^{4-}$ ligands and annealed at 350 °C for 5 sec using rapid thermal annealing (RTA). The transfer characteristics were measured at V_{DS} = 2 V and the linear regime mobility was calculated from the transconductance. The channel length and width are L = 150 μm, W=1500 μm, respectively. **d)** The absorption spectrum of the annealed InAs NC film. The arrows denote laser lines used for photoconductivity measurements. **e)** Bias dependence for the dark current and the photocurrent excited with 980 nm and 1310 nm illumination of InAs NCs film. **f)** Photoresponse of InAs NC layers measured at different excitation wavelengths at 2 V bias applied across 150 μm long channel.

ing an amorphous matrix encapsulating the nanoparticles. The intrinsic electronic properties of the isolated NC are greatly modified in the matrix, whose atomistic structure plays a key role in enabling efficient electronic transport. The structural model derived here permitted to explain the origin of the measured negative photoconductivity of the nanocomposite.

We carried out *ab initio* thermodynamics calculations for extended surfaces of InAs in contact with Sn_xS_y, with various orientations and compositions, in order to establish their stability as a function of preparation conditions. Key predictions gained from this study were validated by experiments, i. e. XPS core level shifts and Raman measurements. We then employed the validated structural motifs to model surfaces of embedded NPs, and to define configurations from which we started *ab initio* molecular dynamics (MD) simulations and generated refined structural models. This approach allowed us to understand the influence of complex configurations formed at the interface and within the embedding matrix, e. g. the formation of sulfur chains, and to study the influence of the matrix density and stoichiometry on the nanocomposite electronic properties.

Fig. 2a illustrates the commonly used concept of ligands adsorbed as intact structural units. Nuclear magnetic resonance experiments indicate that some intact ligands are indeed present on the NC surface [29]. However, according to our *ab initio* calculations, $Sn_2S_6^{-4}$ dissociates without any barrier on the bare InAs(100) and (111) surfaces, which are the most probable orientations on faceted InAs NCs. Rapid dissociation was also found in the case of superlattices of InAs and $Sn_2S_6^{4-}$ where both ends of the ligand were bound to two InAs surfaces. Thus the information gained from existing NMR studies and *ab initio* calculations led to the hypothesis that first some ligands decompose at the InAs surface leading to the formation of a passivation layer, and it is on top of this layer that additional intact ligands may adsorb.

To characterize the interface between the NC and the surrounding layer of decomposed ligands, we considered a variety of structural candidates and processes: (i) NC surface reconstructions, (ii) (partial) dissociation of the ligands on the surface, (iii) diffusion of ligand constituents on the NC surface and subsurface incorporation, (iv) formation of S, InS, or SnS films on the NC surface, (v) combinations of i-iv, (vi) adsorption of ligands on passivating layers, (vii) heat treatment to obtain embedded NCs in amorphous matrices at various stoichiometries and densities. The relative stability of the resulting structural models were evaluated by calculating the respective interface energies from *first principles*, choosing the chemical potentials to mimic different synthesis and growth conditions (see Fig. 2).

We identified a class of minima with lowest energy, differing by just a few meV/$\mathring{A}^2$. We thus expect a statistical distribution of these structural motifs to be present in the nanocomposite, depending on synthesis conditions (chemical potentials). Almost all low energy interface structures are characterized by InAs surfaces passivated by sulfur, which is not surprising, as sulfur is commonly used to passivate bulk III-V semiconductors [30–35] and InAs nanowires [36]. However for very low sulfur chemical potentials, Sn-induced surface reconstructions become the lowest energy configurations (cf. gray areas in Fig 2b-d). At higher sulfur chemical potentials, we observed an additional effect: sulfur displaces As and it is incorporated into the subsurface layer. The adsorption of intact Sn_2S_6 units on the S-passivated surfaces becomes possible, leading to a local energy minimum. However Sn_2S_6 is unstable towards dissociation into SnS_4 tetrahedral units, and the most stable structural motifs identified in our calculations consist of S-passivated NCs embedded in amorphous SnS_x matrices.

To confirm our predicted sub-surface sulfur incorporation, we carried out Angle Resolved X-ray Photoelectron Spectroscopy (ARXPS) measurements previously employed to study the effect of sulfidation on bulk InP surfaces [39, 40]. We used the surface of bulk InAs(111)

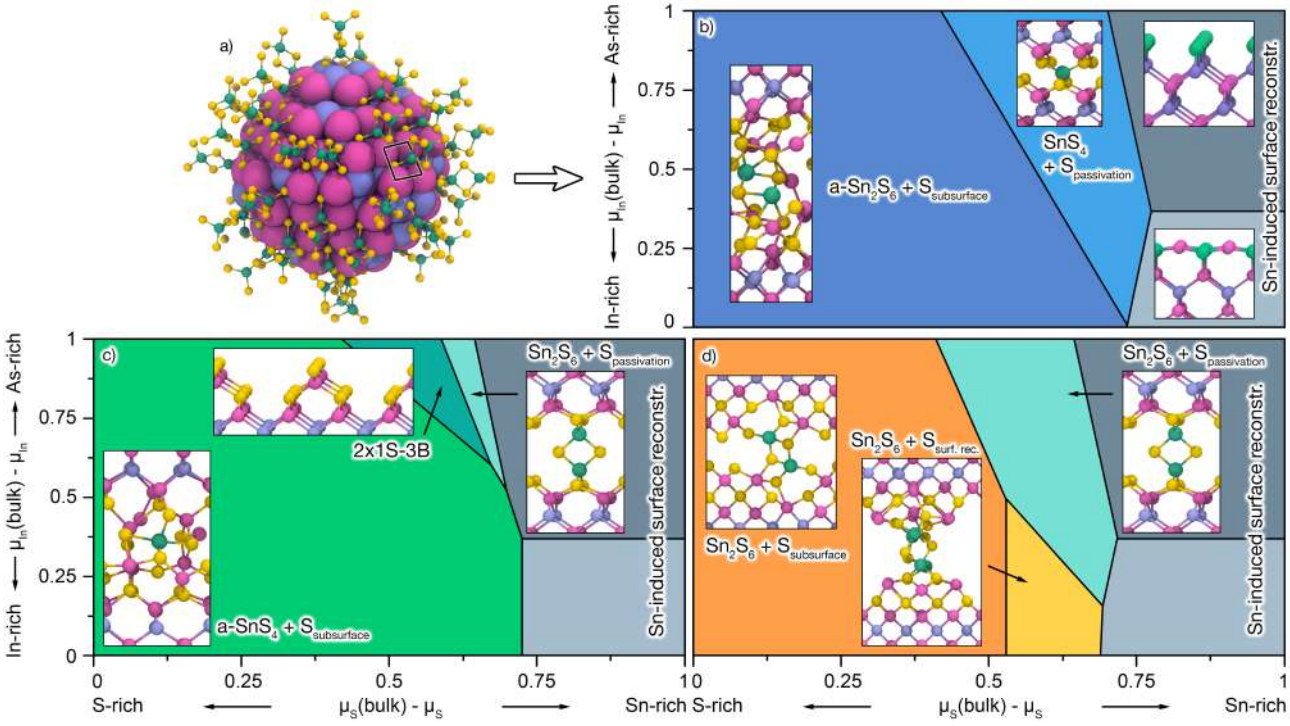

Figure 2. **a)** Idealized model of faceted InAs NC capped with intact $Sn_2S_6^{4-}$ ligands. Magenta, violet, turquoise and yellow spheres denote In, As, Sn and S atoms, respectively. **b-d)** Energy diagrams for interfaces between InAs(001) and $Sn_2S_6^{4-}$ ligands, computed from first principles using density functional theory, with lowest energy structures shown in b, and the next ones higher in energy in c and d, in order of decreasing stability. Corresponding diagrams for the (111) surface orientation are included within the supplementary information (cf. Fig. S3). The chemical potentials μ_{In} and μ_{As} were varied between the In-rich [$\mu_{In} = \mu_{In}(bulk)$] and As-rich [$\mu_{As} = \mu_{As}(bulk)$] conditions of InAs formation [$\mu_{In} + \mu_{As} = \mu_{InAs}(bulk)$]. In a similar fashion, μ_{Sn} and μ_S were varied between Sn-rich [$\mu_{Sn} = \mu_{Sn}(bulk)$] and S-rich [$\mu_S = \mu_S(bulk)$] conditions of SnS_2 formation [$\mu_{Sn} + 2 \cdot \mu_S = \mu_{SnS_2}(bulk)$]. When using hydrazine as solvent, μ_H may vary between H-rich [$\mu_H = \mu_H(H_2)$] and N-rich [$\mu_N = \mu_N(N_2)$] conditions of hydrazine formation [$\mu_N + 2 \cdot \mu_H = 1/2\ \mu_{N_2H_4}$]. Models containing hydrogen at the NC-ligand interface were found to be mostly unstable, even at H-rich conditions.

wafers treated with $(NH_4)_2S$ as a model system for the NC surfaces of interest. We found that the As signal decreases linearly with increasing angles suggesting a homogenous distribution of As in the sample, as a function of depth. However the S 2p core signal shows two distinct profiles on either side of 55 degrees. At angles smaller than 55 degrees, when the sampling depth reaches below the surface, the signal intensity decreases linearly, with a slope smaller than that of As, showing a significantly higher concentration of S as compared to As in that region of the material. At angles larger than 55 degrees, when the signal is coming exclusively from the surface, the S 2p signal intensity sharply increases, suggesting that the majority of sulfur is not concentrated at but slightly below the surface. These findings confirm the prediction obtained from *first principles* calculations about surface passivation layers originating from ligand dissociation, with S diffusion into the NC sub-surface region being one of the main passivation mechanisms.

In this context, it should be noted that dissociation of the ligands occurs in two conceptually different circumstances: (i) the ligand decomposition described herein at the NC surfaces and concurrent formation of passivation layers upon ligand exchange is unintentional and surprising, (ii) on the other hand, decomposition of the ligands is used intentionally when preparing all-inorganic NC solids by inkjet printing or spin-coating. Upon subsequent drying, a matrix encapsulating the NCs is formed from the hydrazinium stannate ligands according to the reaction $(N_2H_5)_4Sn_2S_6 \rightarrow SnS_2 + 4\ N_2H_4 + 2\ H_2S$. H_2S and N_2H_4 leave the system, so that an SnS_2 matrix encapsulating the InAs NCs is retained. The matrix structure is amorphous and the average surface to surface distance between neighbouring nanocrystals is approximately 0.5 nm, demonstrated by powder x-ray diffraction and transmission electron microscopy (cf. Figs. S1 and S2).

To prove the ligand decomposition of type (i) and concurrent subsurface sulfur formation also in the case of all-inorganic NC solids, we turned to Raman spectroscopy, which is sensitive to lattice disorder. As-synthesized InAs NCs show characteristic transverse (TO) and longitudinal (LO) optical phonon modes centered at 217 and 236 cm^{-1} respectively (Fig. 3c) [41]. However upon thiostannate ($(N_2H_5)_4Sn_2S_6$) ligand exchange and forming all-

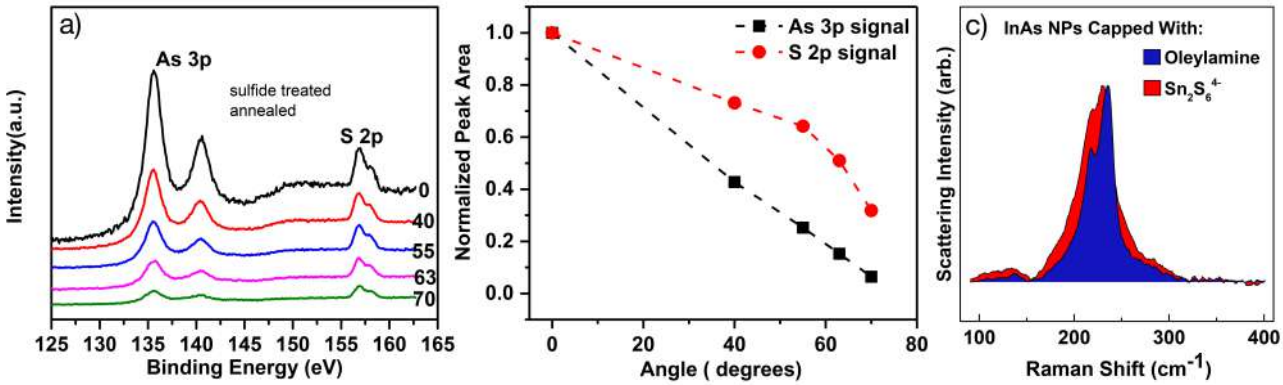

Figure 3. **a)** Measured XPS core level spectra for As 3p and S 2p regions for an InAs(111) wafer treated with $(NH_4)_2S$ and annealed at 350 °C for 30 minutes, taken at different detector angles (0°-70°). **b)** Normalized integrated peak areas for As 3p and S 2p core levels as a function of detector angle calculated from the data in a).The ARXPS technique used here is surface sensitive because only photoelectrons generated within a certain escape depth reach the detector without a loss of their initial kinetic energy. Further profiling of the surface can be done if the emitted photo-electrons are collected at a grazing emission angle. The escape depth of the photo-electrons being collected decreases with increasing angle: $x = d \cdot cos\ \theta$, where θ is the angle between the detector and the normal to the surface and d is the initial escape depth. At $\theta = 0°$ the detector is positioned directly normal to the surface and therefore the escape depth assumes its maximum value. The integrated peak areas of the As 3p and the S 2p signal as a function of detector angle are shown in Fig. 3b. **c)** Raman spectra of InAs nanocrystals capped with organic ligands (red) and with $(N_2H_5)_4Sn_2S_6$) ligands. Broadening of the TO and LO phonon modes is observed upon capping with thiostannate ligands and forming all-inorganic NC solids by solution casting.

inorganic NC solids by solution casting and subsequent drying of the NC film, we observed a clear broadening of both features along with a slight shift of the LO phonon to lower wave-numbers. Such a broadening is indicative of some lattice disorder in the nanocrystal beyond mere surface reconstruction [42]. A similar broadening of the Raman peaks has been observed upon ion bombardment in bulk III-V semiconductors, e.g. InP and GaAs, leading to the formation of point defects in the lattice [43, 44]. On the contrary, CdSe NCs, which are known to bind to intact thiostannate ligands, do not show significant broadening of the Raman spectra due to ligand exchange [29]. Therefore our Raman measurements provide further confirmation that sulfur is not merely present on the NC surfaces and in the surrounding matrix, but is also incorporated into the subsurface sites.

In order to utilize the identified lowest energy structural motifs, validated by experiments, and "transfer" them from extended interfaces to NC surfaces, we performed *ab initio* MD simulations where these motifs were explicitly included as starting points of annealing cycles. We accounted for variations in the density and stoichiometry of the amorphous matrix by performing a series of simulations with stoichiometries ranging from SnS to SnS_3 and densities from that of bulk SnS ($\rho = 5.44\ g/cm^3$) to that of surface-adsorbed Sn_2S_6 ($\rho = 2.8\ g/cm^3$, estimated by adsorbing Sn_2S_6 ligands between two InAs slabs at maximum coverage, with no surface dangling bonds). We could identify specific motifs leading to a significant lowering of the total energy of the system upon performing annealing cycles, as shown in Fig. 2. For example, we built models with subsurface sulfur by exchanging As atoms in the NC subsurface layer with S atoms inside the matrix and by performing repeated annealing cycles (cf. Fig. 4c-d). On average, after the completion of an annealing cycle the total energy was decreased by about 1 eV per S-As substitution, confirming the driving force towards diffusion of sulfur into the NCs [38].

Even in MD simulations where motifs identified in our *ab initio* thermodynamic calculations were not explicitly inserted in the system, we found that InAs drew sulfur from the matrix, leading to the formation of a sulfur shell around the NCs and Sn clusters inside the matrix, irrespective of mass density and stoichiometry. In the experiments, however, there is always excess sulfur leaving the system in the form of H_2S. To model a grand-canonical situation as in experiment, we prevented the formation of Sn clusters and corresponding defect states by exchanging some Sn atoms for S and performing repeated annealing cycles. Consistently, our XPS measurements show a complete absence of Sn^0, when examining photoelectrons originating from Sn, and thereby exclude the presence of any Sn clusters.

For matrix mass densities exceeding 3.5 g/cm^3 our MD simulations predicted a uniformly dense amorphous matrix around the NCs. At lower densities we observed instead strand-like structures connecting the NCs, leaving nanopores distributed throughout the matrix. In addition to the density, also the stoichiometry affects significantly the local atomistic structure of the matrix, as reported in Fig. 4.

We now turn to describe the electronic and transport properties of the structural models generated here. Since

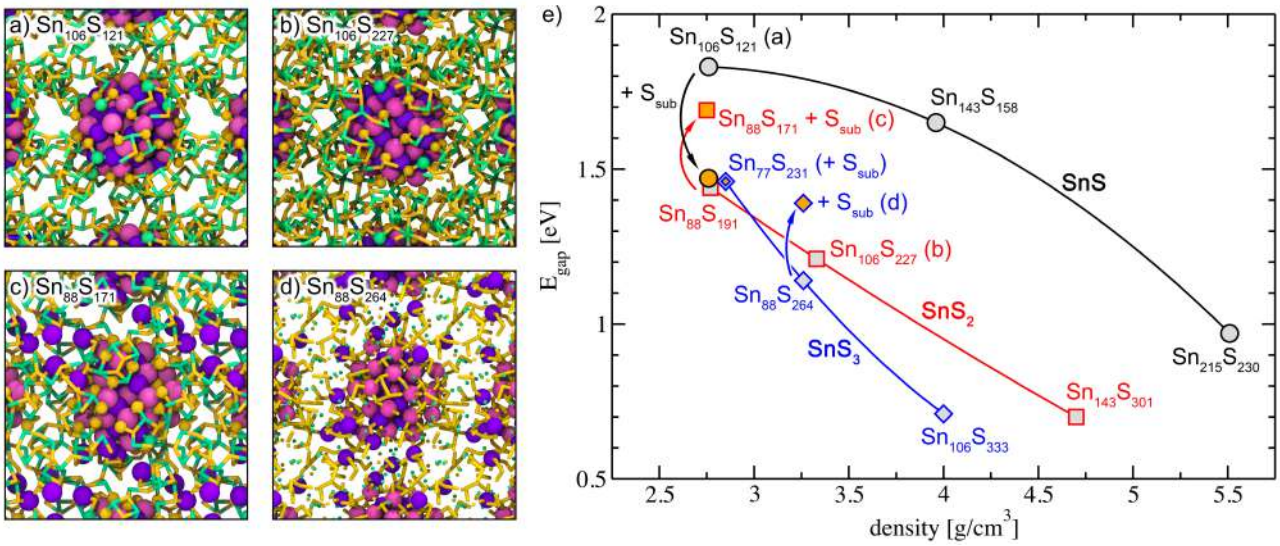

Figure 4. **a)** Schematic representation of a $In_{38}As_{28}$ NC embedded in a dilute amorphous $Sn_{106}S_{121}$ matrix ($\rho_{mat} = 2.8\ g/cm^3$). Magenta and violet spheres, yellow and turquoise rods represent In and As, S and Sn, respectively. Local structural units resemble the 3-fold and 6-fold coordinated Sn-atoms known from the bulk-SnS *Pnma* and *Fm-3m* phases [37]. **b)** $In_{38}As_{28}$ NC embedded in dilute a-SnS_2 at $\rho_{mat} = 3.3\ g/cm^3$. For SnS_2 and higher S contents we observe the formation of sulfur chain structures connecting the NCs, possibly explaining the large mobilities observed in recent experiments [16]. **c)** Lower total energies and larger electronic gaps are obtained by introducing subsurface sulfur and corresponding incorporation of As in the matrix during the MD runs (SnS_2 matrix at $\rho_{mat} = 2.8\ g/cm^3$, (sub-)surface S atoms drawn as yellow spheres). **d)** $In_{38}As_{28}$ embedded in a-SnS_3 at $\rho_{mat} = 3.3\ g/cm^3$, showing both sulfur chains and subsurface sulfur. **e)** Dependence of the NC-composite electronic gap on the matrix density, stoichiometry and matrix atomistic structure (see text). SnS_{1+x} matrices feature many small regions resembling either rocksalt or the 3-fold coordinated Sn units known from the *Fm-3m* and *Pnma* phases of bulk-SnS [37], respectively [38]. Matrices with SnS_{2+x} stoichiometry and $\rho < 3g/cm^3$ are characterized by a mixture of tetrahedral SnS_4 units, as predicted to be a low energy structure in the phase diagram (cf. Fig. 2b) and SnS_3 units in resemblance of the *P-3m1* phase of bulk-SnS_2 [37]. For mass densities $\rho_{mat} > 3\ g/cm^3$ we observed the formation of sulfur chains connecting the NCs (cf. Figs. 4b and 4d).

the bonding in this system is partially ionic and charge transfers are involved, all the electronic properties presented here are computed at the hybrid functional level of theory, using dielectric dependent hybrid functionals [45, 46]. We found a strong dependence of the electronic gap on the matrix density and hence on the synthesis conditions (see Fig. 4e) [47]. The gap is decreased by 0.8 eV, when increasing ρ_{mat} from 2.8 g/cm^3 (interfacial Sn_2S_6) to 5.4 g/cm^3 (bulk-SnS). In addition, increasing the sulfur content led to a gap reduction. However, introducing subsurface sulfur led to a moderate increase of the gap by up to 0.3 eV for NCs embedded in SnS_2 or SnS_3, but to a decrease (0.3 eV) for SnS-embedded NCs.

A number of defect states were identified in the nanocomposites, which play a key role in determining electronic and transport properties. Fig. 5 shows the wavefunction square moduli of the most common ones which arise from SnS_3 groups bound to either (i) neighbouring SnS_3 groups, and forming S dimers, or (ii) directly to the NP surface, in such a way that electron counting rules are not fulfilled; these bonding configurations lead to localized electronic states as shown in Fig. 5a. Sn dangling bonds are another common defect, cf. Fig. 5b. Further defect states arise from corner-sharing SnS_3 and AsS_3 groups, cf. Fig. 5c, and over-coordinated In and Sn atoms.

The relative occurrence of these defects varies strongly depending on the amount of S present in the system. Low S content largely suppresses the presence of As in the matrix, but increases the number of Sn dangling bonds. With increasingly higher S content, neighbouring SnS_3 groups first form S dimers and trimers, cf. Figs. 5a and b. Eventually, these merge into increasingly longer S chain segments, thereby significantly reducing the number of shallow trap states near the VBM and leading to more extended electronic states, cf Fig. 5d. The formation of these chains, which was observed even during our relatively short *ab initio* MD annealing cycles of $\sim$ 15 ps, give rise to a significant number of electronic states close in energy that are delocalized along segments of the chains.

Figs. 6a and b show the band alignment at the nanoparticle-matrix heterojunction for two representative models with low and high S content, respectively. The nano-heterojunctions are always of type II, with the matrix valence band edge located above the NP HOMO. Note the S chain states located close in energy to the valence band edge of the matrix. Analogous to Si NPs

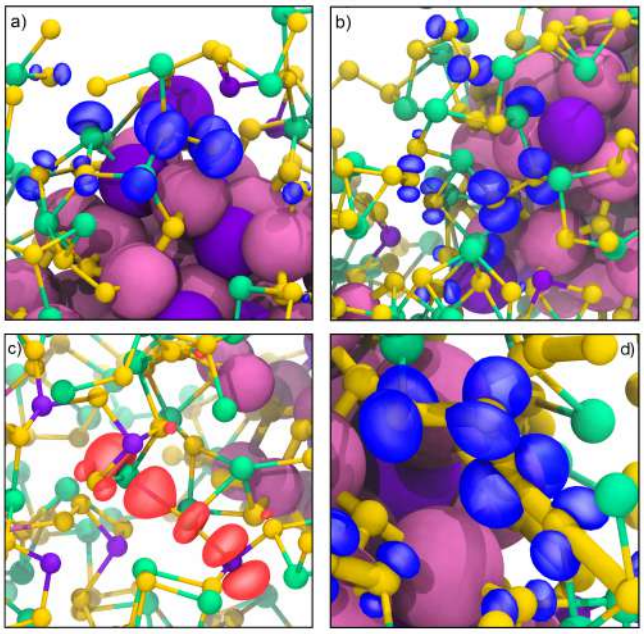

Figure 5. **a-c)** Isodensity plots of the square wavefunction moduli for representative defect states of InAs NCs interfaces with amorphous matrices: SnS_3 groups bound to S dimer and NP surface, respectively (a), undercoordinated Sn with only 2 Sn-S bonds (b), and SnS_3 group bound to matrix-solvated As (c). **d)** Isodensity plots of the square wavefunction moduli for a representative state near the valence band edge associated to a S chain segment. Occupied (empty) states are coloured in blue (red).

embedded in ZnS [9], we expect the formation of charge-separated transport channels due to the type II alignment. Thus, our findings indicate that the unusually high mobilities measured for NCs bridged by sulfur-based MCCs [16] originate from a combination of factors: (i) charge-separated transport channels for electrons and holes and (ii) a type II alignment enabling hopping transport from NC to NC for electrons and band-like transport for holes [48].

Additionally, increasing the matrix stoichiometry towards SnS_3, we predict improved hole transport due to the formation of sulfur chains acting as hole conducting interconnects throughout the matrix and a concurrent reduction of the number of shallow trap states near the matrix VBM. In Fig. 6 we also show the electronic levels associated to characteristic defects. Note the decreased number of defective SnS_3 groups and Sn dangling bond defects in Fig. 6b compared to Fig. 6a, concurrent with sulfur chain formation.

In particular, we note that for the SnS_2 stoichiometry used in our experiments the states induced by matrix-solvated As (Fig. 6a) are consistent with and may well explain the observed negative photoconductivity in this system. The matrix As levels provide the donor states inferred from the Stöckman model presented in Ref. [16], as we discuss below.

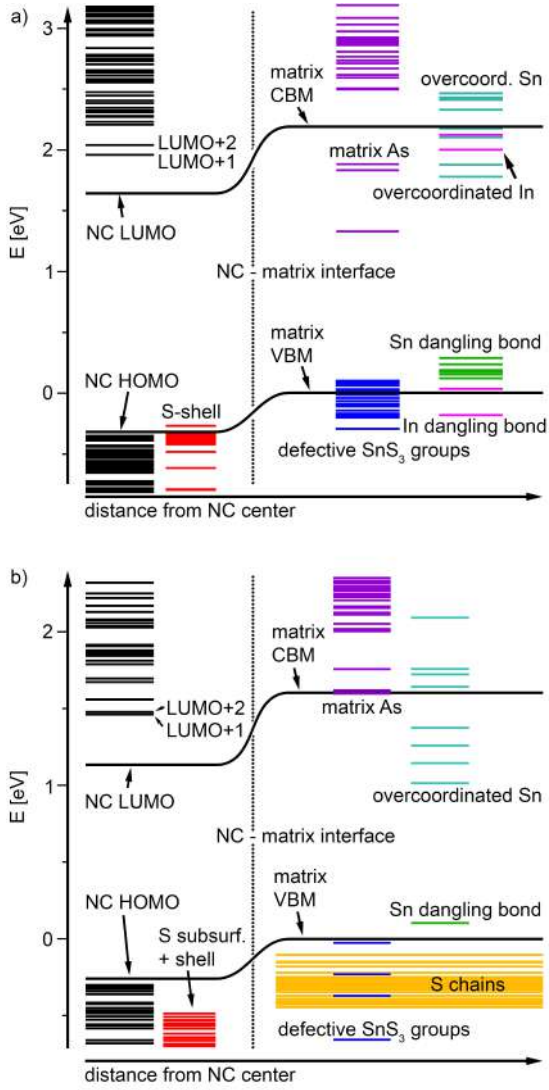

Figure 6. Energy level alignment at nano-heterojunction between $In_{38}As_{28}$ and **a)** $Sn_{88}S_{171}$ and **b)** $Sn_{88}S_{264}$ matrix, computed using density functional theory and dielectric dependent hybrid (DDH) functionals [45, 46]. Both models contain subsurface S incorporated into the NP and in turn As solvated inside the matrix. In terms of defect states, of particular interest are the levels arising from corner-sharing SnS_3 and AsS_3 groups. Thereby As occupies a Sn lattice site, in a configuration which otherwise would fulfill electron counting. Compared to Sn, the additional As electron may be accommodated in, e. g., a Sn dangling bond or SnS_3 defect state, with an empty defect state localized to a SnS_3-AsS_3 unit. Note these defects are located above the NC LUMO. VBM and CBM denote valence and conduction band edges, respectively.

Finally, we examine the unusual transport properties observed in InAs nanocomposites. Mobilities were measured by FET transconductance, cf. Fig 1a-c. According to Fig. 6, exciting the system from the NC highest occupied molecular (HOMO) to the NC lowest unoccupied molecular orbital (LUMO) (cf. Fig. 1d, 1310 nm),

may be responsible for n-type conduction with a relatively high electron mobility (on the order of 4.0 cm^2/Vs according to Fig. 1c). The excited electron can recombine with photoexcited minority carriers (holes) with the rate determined by the band-edge carrier recombination lifetime τ_r, resulting in ordinary positive photoconductivity (cf. Fig. 1f). In contrast, an excitation at a shorter wavelength may promote the electron into the matrix conduction band edge or NC states above the LUMO, e.g. LUMO+1 or LUMO+2 (cf. Fig. 1d, < 980 nm). In ordinary semiconductor NCs, these hot electrons could quickly cool into lower available states via intraband relaxation with the rate constant τ_{intra}^{-1}. However, in InAs NCs with $Sn_2S_6^{4-}$ ligands, the hot electrons may be trapped into a localized state (τ_{trp}^{-1} rate constant) formed by defects, see Fig. 7a. Trapping of hot electrons is common for NCs; e.g., it has been observed in single-NC blinking experiments [49], and it does not lead to negative photoconductivity if trapped electrons quickly recombine. Using a kinetic model for the photoconductivity $\Delta\sigma$ proposed in Ref. [50],

$$\Delta\sigma = Ge\mu_e \left(\tau_r - \frac{\tau_{th}\tau_{dtrp}}{\tau_{trp}} \right), \qquad (1)$$

where G is the photoexcitation rate, we expect electrons may be pocketed in a high-energy state above the mobility edge with long detrapping time τ_{dtrp}, due to defects identified in our structural models. The first term in eq. (1) describes normal (positive) photoconductivity while the second (negative) term becomes dominant when $\tau_{dtrp} >> \tau_r$; $\mu_e >> \mu_h$ is typical for majority and minority carriers in disordered semiconductors, and was indeed observed in our FET experiments.

The localized donor states above the mobility edge are provided by matrix-solvated As. Arsenic preferentially occupies a Sn lattice site, leading to corner-sharing SnS_3 and AsS_3 groups, in a configuration that without As substitution would satisfy electron counting. Compared to Sn, we propose that the additional As electron is accommodated in an acceptor state given by, e. g., a Sn dangling bond or SnS_3 defect state. At the experimental matrix stoichiometry, the empty matrix-As states with lowest energy are often located energetically between the NC LUMO and LUMO+1/+2 states, but below the matrix CBM, see Fig. 6a and Fig. 7a. These donor states are highly localized, cf. Fig. 5c. Ultimately, the origin of these trap states can be traced back to subsurface sulfur formation, which in turn gives rise to matrix-solvated As.

When increasing the stoichiometry to SnS_3 and the matrix mass density by 18%, we predict from our calculations that the same type of defect levels occur, but at higher energies above the matrix CBM, cf. Fig. 6b. Thus no trapping should occur, suppressing the negative photoconductivity. At the same time, the additional sulfur is now forming hole conducting chains throughout the matrix. At present, these synthesis conditions cannot be reached in our experiments and only SnS_2 matrix stoichiometry is possible, leading to the electronic structure shown in Fig. 6a. However, based on our calculations we suggest that designing experiments that would allow for the synthesis of all inorganic NP solids with increased sulfur content beyond SnS_2 is a promising direction of research, and for those systems the negative photoconductivity should be suppressed.

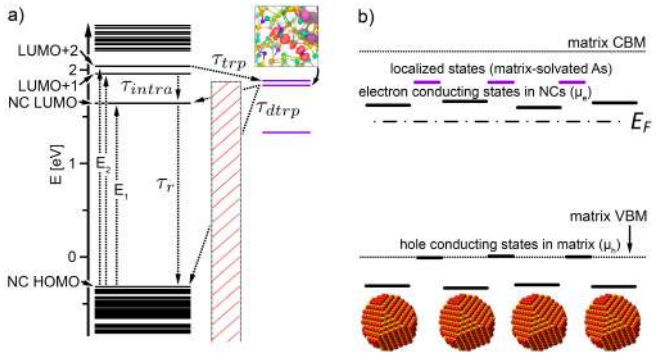

Figure 7. Model of ambipolar photoresponse of InAs NCs with $Sn_2S_6^{4-}$ ligands. **a)** Assignment of the absorption bands of InAs NCs. The first absorption peak at 1310 nm corresponds to the NC HOMO - NC LUMO transition (E_1), while the second absorption peak around 980 nm originates from NC HOMO - NC LUMO+1 and NC HOMO - NC LUMO+2 transitions (E_2). The hot electrons promoted to the LUMO+1/+2 states can undergo intraband relaxation or get trapped by localized states originating from matrix-solvated As, which are situated above the NC LUMO (cf. Fig. 5c). The corresponding characteristic times are described in the text. The electronic levels shown in this model are obtained from our electronic structure calculations and are identical to the ones shown in Fig. 6a). **b)** In the NC film, the mobility edge for majority carriers (electrons) is associated with the NC LUMO states and the hole-conducting states are given by the matrix band edge.

In conclusion, we established an integrated theoretical and experimental strategy to characterize buried interfaces between ligands and nanocrystals in all inorganic nanocomposites. Understanding and controlling these interfaces are of key importance to eventually design nanomaterials with target properties. Starting from configurations predicted from electronic structure calculations, and validated by XPS and Raman experiments, we conducted a series of first principles MD simulations, which allowed us to derive atomistic structural models as a function of synthesis conditions. We found that inorganic ligands are not adsorbed as intact units, but rather they decompose giving rise to an amorphous matrix surrounding the nanoparticles; as a consequence nanocrystals and inorganic ligands may no longer be considered as having separate identities. Instead, a nanomaterial is formed, whose electronic and transport properties depend on the matrix density and defect structure, and ultimately on synthesis conditions. Specifically, we found that Sn_2S_6 ligands deposited on InAs nanocrystals lead to the for-

mation of a (sub-)surface sulfur layer. It is on top of this modified surface that additional ligand adsorption occurs, where temperature-induced decomposition leads to complex atomistic configurations at the nanocrystal-matrix interface and within the matrix itself. These structural motifs include the formation of a sulfur chain network linking the nanocrystals and characteristic defects inside the matrix. We found that the interfaces formed under a variety of conditions are always type-II junctions favourable for electronic transport and charge extraction, and we identified specific defects responsible for the measured negative photoconductivity. The integrated theoretical and computational strategy presented here may be generalized to the study of broad classes of semiconductor nanocomposites and nanoparticle-in-glass systems.

ACKNOWLEDGEMENTS

Mr. Vladislav Kamysbayev helped with the elemental analysis of the samples. V. S. was primarily supported by the University of Chicago Materials Research Science and Engineering Center, which is funded by NSF under award number DMR-1420709. G.G., E. M. J. and D. T. were supported by MICCoM as part of the Computational Materials Sciences Program funded by the U.S. Department of Energy (DOE), Office of Science, Basic Energy Sciences (BES), Materials Sciences and Engineering Division (5J-30161- 0010A). E. S. and S. W. were supported by the German Ministry of Education and Research (BMBF) within the *NanoMatFutur* programme, grant No. 13N12972. Supercomputer time provided by NERSC (project No. 35687) and the Max-Planck Computing and Data Facility, Garching, is gratefully acknowledged.

METHODS

We carried out *first principles* calculations with density functional theory and plane-wave basis sets. The atomistic thermodynamics calculations were were carried out in the local density approximation [51] with Quantum Espresso [52], using ultrasoft pseudopotentials [53] and a wavefunction energy cutoff of 46 Ry. Surface energies γ were computed as

$$\gamma = \left(E_{surf} - \sum_i \mu_i N_i \right) / A, \qquad (2)$$

where μ_i, N_i and A are the chemical potential of species i, number of atoms and surface area, respectively. The choice of chemical potentials mimicked different synthesis and growth conditions: μ_{In} and μ_{As} were varied between the In-rich $[\mu_{In} = \mu_{In}(bulk)]$ and As-rich $[\mu_{As} = \mu_{As}(bulk)]$ conditions of InAs growth $[\mu_{In} + \mu_{As} = \mu_{InAs}(bulk)]$. In a similar fashion, μ_{Sn} and μ_S were varied between Sn-rich $[\mu_{Sn} = \mu_{Sn}(bulk)]$ and S-rich $[\mu_S = \mu_S(bulk)]$ conditions of SnS_2 growth $[\mu_{Sn} + 2 \cdot \mu_S = \mu_{SnS_2}(bulk)]$.

Dangling bonds at the slab bottom were terminated using fractionally charged pseudo-hydrogen. To remove the contribution of the slab bottom to the surface energy we constructed a slab with two equivalent In terminated surfaces, passivated by pseudo-H atoms. From its total energy, the energy of one H-passivated surface was determined and subtracted from the total energy of the InAs(001) surface models. For the InAs(111) surface the top and bottom layers of the slab were not identical. Following Zhang and Wei [54] we used a wedge-shaped geometry with one (001) and two equivalent (111) and $(\bar{1}\bar{1}1)$ surfaces to calculate individual surface energies.

Molecular dynamics simulations were performed with Qbox [55], using optimized norm-conserving pseudopotentials [56], a wavefunction energy cutoff of 80 Ry and the Perdew-Burke-Ernzerhof approximation [57, 58]. We used a dielectric-dependent hybrid (DDH) functional [45, 46] with a mixing parameter of $\alpha = 0.1$ [59] and a slightly reduced wavefunction energy cutoff of 70 Ry to compute the electronic properties of the models obtained from the preceding MD calculations.

Band gaps were calculated as effective quantities, defined with a threshold for the electronic density of states $D(\epsilon)$:

$$\int_{\mathrm{VBM}}^{E_F} D(\epsilon)d\epsilon = \int_{E_F}^{\mathrm{CBM}} D(\epsilon)d\epsilon = \Delta \int_{-\infty}^{E_F} D(\epsilon)d\epsilon, \qquad (3)$$

where E_F is the Fermi energy of the composite system, located inside the gap, and Δ is a suitably chosen threshold parameter to discard midgap and defect states.

DATA AVAILABILITY

The datasets generated and analyzed during the current study are available from the corresponding author on reasonable request.

[1] J. Park, J. Joo, S. Kwon, Y. Jang, and T. Hyeon, Angewandte Chemie International Edition **46**, 4630 (2007).
[2] Y. Yin and A. P. Alivisatos, Nature **437**, 664 (2005).
[3] C. B. Murray, C. R. Kagan, and M. G. Bawendi, Annual Review of Materials Science **30**, 545 (2000), http://dx.doi.org/10.1146/annurev.matsci.30.1.545.

[4] X. Peng, L. Manna, W. Yang, J. Wickham, E. Scher, A. Kadavanich, and A. P. Alivisatos, Nature **404**, 59 (2000).

[5] W. J. Parak, Science **334**, 1359 (2011), http://www.sciencemag.org/content/334/6061/1359.full.pdf.

[6] D. V. Talapin, MRS Bulletin **37**, 63 (2012).

[7] M. V. Kovalenko, CHIMIA International Journal for Chemistry **67**, 316 (2013-05-29T00:00:00).

[8] S. Wippermann, Y. He, M. Vörös, and G. Galli, Applied Physics Review **3**, 040807 (2016).

[9] S. Wippermann, M. Vörös, A. Gali, F. Gygi, G. Zimanyi, and G. Galli, Physical Review Letters **112**, 106801 (2014).

[10] S. Wippermann, D. Vörös, M. Rocca, A. Gali, G. Zimanyi, and G. Galli, Physical Review Letters **110**, 046804 (2013).

[11] M. Vörös, S. Wippermann, B. Somogyi, A. Gali, D. Rocca, G. Zimanyi, and G. Galli, Journal of Materials Chemistry A **2**, 9820 (2014).

[12] M. V. Kovalenko, L. Manna, A. Cabot, Z. Hens, D. V. Talapin, C. R. Kagan, V. I. Klimov, A. L. Rogach, P. Reiss, D. J. Milliron, P. Guyot-Sionnest, G. Konstantatos, W. J. Parak, T. Hyeon, B. A. Korgel, C. B. Murray, and W. Heiss, ACS Nano **9**, 1012 (2015), pMID: 25608730, http://dx.doi.org/10.1021/nn506223h.

[13] M. A. Boles and D. V. Talapin, Science **344**, 1340 (2014), http://www.sciencemag.org/content/344/6190/1340.full.pdf.

[14] C. A. Leatherdale, C. R. Kagan, N. Y. Morgan, S. A. Empedocles, M. A. Kastner, and M. G. Bawendi, Phys. Rev. B **62**, 2669 (2000).

[15] M. V. Kovalenko, M. I. Bodnarchuk, J. Zaumseil, J.-S. Lee, and D. V. Talapin, Journal of the American Chemical Society **132**, 10085 (2010).

[16] W. Liu, J.-S. Lee, and D. V. Talapin, Journal of the American Chemical Society **135**, 1349 (2013), pMID: 23267673, http://dx.doi.org/10.1021/ja308200f.

[17] J.-S. Lee, M. V. Kovalenko, J. Huang, D. S. Chung, and D. V. Talapin, Nat Nano **6**, 348 (2011).

[18] A. H. Ip, S. M. Thon, S. Hoogland, O. Voznyy, D. Zhitomirsky, R. Debnath, L. Levina, L. R. Rollny, G. H. Carey, A. Fischer, K. W. Kemp, I. J. Kramer, Z. Ning, A. J. Labelle, K. W. Chou, A. Amassian, and E. H. Sargent, Nat Nano **7**, 577 (2012).

[19] Z. Ning, Y. Ren, S. Hoogland, O. Voznyy, L. Levina, P. Stadler, L. Xinzheng, D. Zhitomirsky, and E. Sargent, Advanced Materials **24**, 6295 (2012).

[20] C. Kagan, E. Lifshitz, E. Sargent, and D. Talapin, Science **353**, 885 (2016).

[21] F. Fan, O. Voznyy, R. Sabatino, C. Bicanic, M. Adachi, J. McBride, R. Quintero-Bermudez, M. Saravanapavanantham, M. Liu, M. Korkusinski, P. Hawrylak, V. Klimov, S. Rosenthal, S. Hoogland, and E. Sargent, Nature **544**, 75 (2017).

[22] J.-S. Lee, M. V. Kovalenko, J. Huang, D. S. Chung, and D. V. Talapin, Nat Nano **6**, 348 (2011).

[23] D. S. Chung, J.-S. Lee, J. Huang, A. Nag, S. Ithurria, and D. V. Talapin, Nano Letters **12**, 1813 (2012), pMID: 22385132, http://dx.doi.org/10.1021/nl203949n.

[24] J. Huang, W. Liu, D. S. Dolzhnikov, L. Protesescu, M. V. Kovalenko, B. Koo, S. Chattopadhyay, E. V. Shenchenko, and D. V. Talapin, ACS Nano **8**, 9388 (2014), pMID: 25181260, http://dx.doi.org/10.1021/nn503458y.

[25] A. A. Cordones, M. Scheele, A. P. Alivisatos, and S. R. Leone, Journal of the American Chemical Society **134**, 18366 (2012), pMID: 23072613, http://dx.doi.org/10.1021/ja3071732.

[26] A. Llordes, G. Garcia, J. Gazques, and D. Milliron, Nature **500**, 323 (2013).

[27] S. Yakunin, D. Dirin, L. Protesescu, M. Sytnyk, S. Tollabimazraehno, M. Humer, F. Hackl, T. Fromherz, M. Bodnarchuk, M. Kovalenko, and W. Heiss, ACS Nano **8**, 12883 (2014).

[28] A. Ekimov, Journal of Luminescence **70**, 1 (1996).

[29] L. Protesescu, M. Nachtegaal, O. Voznyy, O. Borovinskaya, A. J. Rossini, L. Emsley, C. Coperet, D. Günther, E. H. Sargent, and M. V. Kovalenko, Journal of the American Chemical Society **137**, 1862 (2015).

[30] J.-F. Fan, H. Oigawa, and Y. Nannichi, Japanese Journal of Applied Physics **27**, L1331 (1988).

[31] M. V. Lebedev, T. Mayer, and W. Jaegermann, Surface Science **547**, 171 (2003).

[32] V. Bessolov and M. Lebedev, Semiconductors **32**, 1141 (1998).

[33] D. Petrovykh, M. Yang, and L. Whitman, Surface Science **523**, 231 (2003).

[34] T. L'vova, I. Sedova, M. Dunaevskiĭ, A. Karpenko, V. Ulin, S. Ivanov, and V. Berkovits, Physics of the Solid State **51**, 1114 (2009).

[35] D. Y. Petrovykh, J. M. Sullivan, and L. J. Whitman, Surface and Interface Analysis **37**, 989 (2005).

[36] D. B. Suyatin, C. Thelander, M. T. Björk, I. Maximov, and L. Samuelson, Nanotechnology **18**, 105307 (2007).

[37] L. A. Burton and A. Walsh, Journal of Physical Chemistry C **116**, 24262 (2012).

[38] Overall, the unit cells in the simulations are always charge neutral, but local units may be charged.

[39] T. Chasse, A. Chasse, H. Peisert, and P. Streubel, Applied Physics A: Materials Science and Processing **65**, 543 (1997).

[40] D. Gallet and G. Hollinger, Applied Physics Letters , 982 (1993).

[41] V. Srivastava, E. M. Janke, B. T. Diroll, R. D. Schaller, and D. V. Talapin, Chemistry of Materials **28**, 6797 (2016).

[42] The Raman signal is much more intense for InAs due to resonance effects and therefore no signature of the thiostannate ligands is seen in the presence of InAs NCs.

[43] C. R. Rao, S. Sundaram, R. Schmidt, and J. Comas, Journal of Applied Physics **54**, 1808 (1983).

[44] E. Bedel, G. Landa, R. Carles, J. Renucci, J. Roquais, and P. Favennec, Journal of Applied Physics **60**, 1980 (1986).

[45] J. H. Skone, M. Govoni, and G. Galli, Phys. Rev. B **89**, 195112 (2014).

[46] J. Perdew, M. Ernzerhof, and K. Burke, Journal of Chemical Physics **105**, 9982 (1996).

[47] The present experiments are restricted to matrix densities and stoichiometries forming at ambient pressure. See Fig. S4 for a comparison between optical absorption spectra of inorganic ligand capped quantum dots in solution to all-inorganic quantum dot solids.

[48] Depending on NC size distribution and packing morphology, the electronic states may localize on individual NCs (weak coupling limit) or form extended states (strongly coupled NC solid). Since the barriers for electrons exiting the nanocrystals into the matrix are high, we assume that at the measured NC surface to surface distance of 0.5 nm there is some coupling between neighboring NCs

in our all-inorganic quantum dot solids.
[49] C. Galland, Y. Ghosh, A. Steinbruck, M. Sykora, J. A. Hollingworth, V. I. Klimov, and H. Htoon, Nature **479**, 203 (2011).
[50] Y. Yang, X. Peng, H.-S. Kim, T. Kim, S. Jeon, H. K. Kang, W. Choi, J. Song, Y.-J. Doh, and D. Yu, Nano Letters **15**, 5875 (2015).
[51] J. P. Perdew and A. Zunger, Phys. Rev. B **23**, 5048 (1981).
[52] P. Giannozzi, S. Baroni, N. Bonini, M. Calandra, R. Car, C. Cavazzoni, D. Ceresoli, G. L. Chiarotti, M. Cococcioni, I. Dabo, A. D. Corso, S. de Gironcoli, S. Fabris, G. Fratesi, R. Gebauer, U. Gerstmann, C. Gougoussis, A. Kokalj, M. Lazzeri, L. Martin-Samos, N. Marzari, F. Mauri, R. Mazzarello, S. Paolini, A. Pasquarello, L. Paulatto, C. Sbraccia, S. Scandolo, G. Sclauzero, A. P. Seitsonen, A. Smogunov, P. Umari, and R. M. Wentzcovitch, Journal of Physics: Condensed Matter **21**, 395502 (2009).
[53] A. M. Rappe, K. M. Rabe, E. Kaxiras, and J. D. Joannopoulos, Phys. Rev. B **41**, 1227 (1990).
[54] S. B. Zhang and S.-H. Wei, Phys. Rev. Lett. **92**, 086102 (2004).
[55] F. Gygi, IBM Journal of Research and Development **52**, 137 (2008).
[56] M. Schlipf and F. Gygi, Computer Physics Communications **196**, 36 (2015).
[57] J. Perdew, K. Burke, and M. Ernzerhof, Physical Review Letters **77**, 3865 (1996).
[58] J. Perdew, K. Burke, and M. Ernzerhof, Physical Review Letters **78**, 1396 (1997).
[59] The measured high frequency dielectric constants $\epsilon(\infty)$ for bulk InAs and SnS_2 are 12.3 and 8.78, respectively.